INTERNATIONAL JOURNAL FOR NUMERICAL METHODS IN FLUIDS
Int. J. Numer. Meth. Fluids 2007; **53**:1689–1706
Published online 10 October 2006 in Wiley InterScience (www.interscience.wiley.com). DOI: 10.1002/fld.1378

Direct numerical simulation of spanwise rotating turbulent channel flow with heat transfer

Nan-Sheng Liu[‡] and Xi-Yun Lu[*, †]

Department of Modern Mechanics, University of Science and Technology of China, Hefei, Anhui 230026, People's Republic of China

SUMMARY

Direct numerical simulation of spanwise rotating turbulent channel flow with heat transfer has been performed. The objective of this study is to reveal the effect of system rotation on the characteristics of turbulent flow, heat transfer, and large-scale motions in rotating turbulence. The Reynolds number is 194, the Prandtl number is 0.71, and the rotation number varies from 0 to 7.5, based on the global friction velocity, the channel half-height, and the angular speed of the spanwise rotating channel. To elucidate the effect of rotation on turbulent flow and heat transfer behaviours, some typical statistical quantities, including the mean velocity, temperature and their fluctuations, turbulent heat fluxes, and the structures of the velocity and temperature fluctuations, are analysed. The budget terms in the transport equation of turbulent heat flux are examined to deal with the effect of Coriolis force on turbulent heat transfer. Since rotational-induced Taylor–Görtler-like large-scale counter-rotating streamwise vortices (i.e. the roll cells) occur, the decomposition of the instantaneous temperature variance and turbulent heat flux is used to reveal the role of the rotational-induced structures on the thermal statistics. Copyright © 2006 John Wiley & Sons, Ltd.

Received 15 January 2006; Revised 18 August 2006; Accepted 22 August 2006

KEY WORDS: direct numerical simulation; spanwise rotating channel flow; heat transfer; thermal statistics; turbulence budget; coherent structure

1. INTRODUCTION

Rotating turbulent flows with heat transfer are of great importance in a variety of engineering applications, such as those in the gas turbine blade passages, pumps, compressors, cyclone

*Correspondence to: Xi-Yun Lu, Department of Modern Mechanics, University of Science and Technology of China, Hefei, Anhui 230026, People's Republic of China.
†E-mail: xlu@ustc.edu.cn
‡E-mail: lns@ustc.edu.cn

Contract/grant sponsor: National Natural Science Foundation of China; contract/grant numbers: 10302028, 90405007

separators, and rotating heat exchangers. In these flows, the rotational-induced additional body forces, i.e. centrifugal and Coriolis forces, acting on the turbulent structures, so that the momentum and heat transfer mechanisms become more complicated [1, 2]. Thus, a physical understanding of turbulent flow and heat transfer in rotating system is desired. Usually, a rotating turbulent channel flow with heat transfer is an appropriate case due to its simple geometry.

Turbulent flow in a spanwise rotating channel is characterized by the rotational-dependent turbulence level, which is enhanced on the pressure side and reduced on the suction side. As a result, the asymmetric distributions of the mean flow and Reynolds stresses about the central line of the rotating channel are observed [3–8]. Meanwhile, the large-scale roll cells are generated due to the Taylor–Görtler instability and shift towards the pressure wall as the rotation rate increases [3, 6]. Consequently, the cross-sectional secondary flow induced by the roll cells contributes to transporting the vorticity fluctuations and turbulent kinetic energy from the pressure side to the suction side. When the rotation rate increases further, turbulence level on the pressure side is reduced significantly, and the large-scale roll cells become much weaker and eventually disappear due to the thickening of the relaminarized region on the suction side [7]. To examine the contributions of the secondary flow induced by the large-scale roll cells to turbulent kinetic energy, the instantaneous velocity fluctuations are decomposed into the contributions from the roll cells and real turbulent fluctuations [6]. However, the effect of the large-scale roll cells on turbulent heat transfer in the rotating channel flow has never been examined but is highly desired.

It is well established that direct numerical simulation (DNS) approach is effective to explore the turbulent transport mechanism of heat transfer between fluid and a solid wall and to provide detailed turbulence and thermal statistics. Thus, some DNS on turbulent heat transfer in the channel flows at relatively low Reynolds and Prandtl numbers have been performed [9–15]. The determination of the thermal budget terms in the transport equations of turbulent heat fluxes is of significant importance to the closures of the turbulent heat fluxes. Kawamura *et al.* [9, 10] have found that the temperature–pressure gradient correlation is a dominant term in the budget of wall-normal turbulent heat flux, while the dissipation rate is small. Nagano and Hattori [11, 16] have indicated that the turbulent diffusion and dissipation terms in the budgets of turbulent heat fluxes are physically meaningful to the construction and assessment of turbulence model involving heat transfer. Thus, it is highly tempting to investigate the rotation effect on the budget terms of turbulent heat fluxes based on DNS data, especially in the aspect of the turbulent heat flux closure for the rotating turbulence.

Although some experimental and numerical investigations have been performed on rotating channel flows, most of them are mainly limited to the turbulence statistics, the near-wall structures, and the dynamic process related to the turbulence energy subject to system rotation without heat transfer [3–8]. Understanding the effects of system rotation on turbulent heat transfer in the rotating channel flow is a fundamental issue in turbulence modelling because any model aimed at predicting the thermal statistics in rotating turbulence should reproduce the essential features of this canonical situation. To our knowledge, however, very few studies are documented to clarify the effect of rotation on the thermal statistics and the dynamic processes of turbulent heat transfer in the rotating channel flow. Here, the turbulent heat transfer in a spanwise rotating channel flow is investigated to reveal the characteristics of turbulence and heat transfer by means of DNS. This work is mainly aimed to study the rotational-dependent behaviours of turbulent flow and heat transfer statistics, and to examine the effect of system rotation on the dynamic process for the generation of turbulent heat flux based on the budget analysis. Furthermore, the decomposition approach [6] is employed to analyse the influence of the rotational-induced large-scale roll cells on the thermal statistics.

DOI: 10.1002/fld

Based on our calculations, some novel behaviours relevant to turbulent heat transfer have been revealed and analysed in the following.

This paper is organized as follows. The mathematical formulation is described in Section 2. The numerical method is briefly given in Section 3. In Section 4, some typical statistical quantities, including the turbulence and thermal statistics, the budget terms in the turbulent heat flux subject to system rotation, and the influence of the rotational-induced large-scale roll cells on the thermal statistics, are discussed. Finally, concluding remarks are summarized in Section 5.

2. MATHEMATICAL FORMULATIONS

The incompressible Navier–Stokes and energy equations are used for the simulation of a spanwise rotating turbulent channel flow with heat transfer, as shown in Figure 1. To normalize the governing equations, the global friction velocity u_τ is used as the velocity scale, the channel half-height h as the length scale, and the temperature difference ΔT between the upper and lower walls as the temperature scale. The non-dimensional governing equations are given as

$$\frac{\partial u_i}{\partial x_i} = 0 \tag{1}$$

$$\frac{\partial u_i}{\partial t} + \frac{\partial (u_i u_j)}{\partial x_j} = -\frac{\partial p}{\partial x_i} + \delta_{1i} + \frac{1}{Re_\tau}\frac{\partial^2 u_i}{\partial x_j \partial x_j} - N_\tau \varepsilon_{ijk}\frac{\Omega_j}{\Omega}u_k \tag{2}$$

$$\frac{\partial T}{\partial t} + \frac{\partial (T u_j)}{\partial x_j} = \frac{1}{Re_\tau Pr}\frac{\partial^2 T}{\partial x_j \partial x_j} \tag{3}$$

where p represents the effective pressure combined with the centrifugal force. The non-dimensional parameters in this problem are the rotation, Reynolds and Prandtl number, which are defined as $N_\tau = 2\Omega h/u_\tau$, $Re_\tau = u_\tau h/\nu$, and $Pr = \nu/\kappa$, respectively, with Ω being the angular speed of rotating frame, ν the kinematic viscosity, and κ the thermal diffusivity. The global friction velocity u_τ

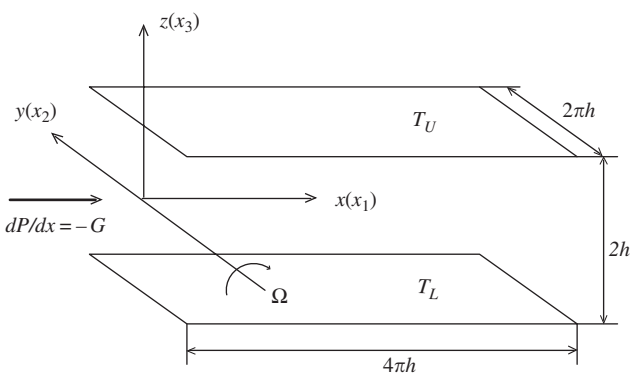

Figure 1. Sketch of the spanwise rotating channel flow with heat transfer.

DOI: 10.1002/fld

is defined as $u_\tau = (|(h/\rho)(\mathrm{d}\bar{p}/\mathrm{d}\bar{x})|)^{1/2}$ [6], where $\mathrm{d}\bar{p}/\mathrm{d}\bar{x}$ is the dimensional pressure gradient to drive the turbulent channel flow.

The flow and temperature fields are assumed to be statistically homogeneous in the streamwise and spanwise directions. Thus, periodic boundary conditions are employed in both the directions. No-slip boundary condition is used on the channel walls. Two different constant temperatures, i.e. $T_\mathrm{U} = 0.5$ and $T_\mathrm{L} = -0.5$, are imposed at the upper and lower walls, respectively. Heat transfer computation is started after the flow field has statistically reached the fully developed turbulent state. Initial temperature field is set to be a linear distribution along the wall-normal direction and homogeneous in the plane parallel to the wall. Then, thermal statistical quantities are calculated after the thermal field has reached the statistically steady state.

3. NUMERICAL METHODS

To solve Equations (1)–(3), a fractional-step method [17], i.e. a variant of the approximate projection method, is employed. Spatial derivatives are discretized by the second-order central difference. Time advancement is carried out by the semi-implicit scheme using the Crank–Nicholson scheme for the viscous terms and the three-stage Runge–Kutta scheme for the convection terms. Details of the discretized formulations were given in [17]. This method simplifies the boundary condition of the non-solenoidal velocity field, while the remaining features of the algorithm proposed by Kim and Moin [18] and Rain and Moin [19], and has the additional advantage that the minimum amount of computer run-time memory is realized.

In this study, the Reynolds number Re_τ is 194, the Prandtl number Pr is 0.71, and the rotation number varies from 0 to 7.5. The grid number is $193 \times 129 \times 161$ with the corresponding computational domain $4\pi h \times 2\pi h \times 2h$ in the streamwise, spanwise, and wall-normal directions, respectively. According to the present test and previous work [6, 20], this grid system is capable of resolving all the essential scales of the turbulence. A stretching transformation is employed to increase the grid resolution in the wall regions. The grid point closest to the wall is located at $z^+ = 0.3$ approximately, while the largest spacing is about $\Delta z^+ = 4.5$ at the centre of the channel, where z^+ is defined as $z^+ = (1 - |z/h|)Re_\tau$. Uniform grids are employed in both the streamwise and spanwise directions with the grid spacing $\Delta x^+ = 12.6$ and $\Delta y^+ = 9.5$, respectively. It has been verified that the computational domain used is large enough by examining the two-point correlation of the velocity fluctuation [21]. To demonstrate that the computed results are independent of the grid resolution, as a typical case, the results calculated by different grid numbers are shown in Figure 2 for the turbulence intensities at $N_\tau = 7.5$.

It is worthwhile to mention that the performance and reliability of the numerical method employed in this study have been verified extensively based on the DNS of rotating and non-rotating turbulent pipe flows [22–24]. It is ensured that the second- and higher-order turbulence statistics compared well with the available DNS results calculated by the spectral methods and with experimental data. Furthermore, the finite difference schemes with second-order accuracy are widely used in the DNS of turbulent and transitional flows, e.g. the rotating channel flow [6, 25], the annular pipe flow [26], the oscillatory flow in the boundary layer and pipe [27, 28], and the turbulent Rayleigh–Bénard convection flow [29]. All the above work confirms that the numerical approach with the second-order accuracy scheme is capable of reasonably predicting the turbulence characteristics. Meanwhile, the relevant code and method used here has been verified based on the extensive investigations of turbulent flow and heat transfer in our previous work [30–37], in

DOI: 10.1002/fld

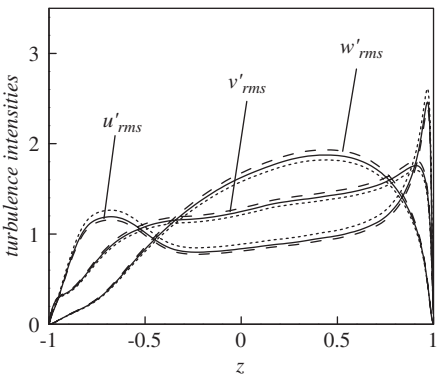

Figure 2. Validation for turbulence intensities at N_τ=7.5 by different grid numbers. Here, dotted lines denote the results calculated by $256 \times 197 \times 197$, solid lines by $193 \times 129 \times 161$, and dashed lines by $129 \times 97 \times 129$.

particular, for the wall-normal rotating turbulent channel flow with heat transfer [21, 38]. Thus, it is ensured that the present DNS is reliable to predict the turbulence and heat transfer behaviours in the rotating channel flow.

4. RESULTS AND DISCUSSION

4.1. Turbulence statistics

To exhibit the turbulent flow behaviour in the rotating channel and to validate the present DNS, Figures 3 and 4 show the mean velocity and turbulence intensities in comparison with previous DNS results [6]. The profiles of the mean velocity are exhibited in Figures 3(a) and (b), where the angular bracket $\langle\,\rangle$ represents the average in time and in the plane parallel to the wall. As shown in Figure 3(a), the profile is symmetric about the central line $z=0$ for $N_\tau=0$, while the profiles become increasingly asymmetric as N_τ increases. The mean velocity profiles for $N_\tau=0$, 3, and 7.5 are compared well with the previous data [6]. By view of the mean velocity profiles, the wall shear of the rotating channel flow, compared with that for $N_\tau=0$, is enhanced near the pressure wall and reduced near the suction wall, indicating the destabilization of flow near the pressure wall and stabilization of flow near the suction wall, respectively. Correspondingly, as shown in Figure 3(b), the changes of the wall law of the mean velocity due to the presence of the spanwise rotation is clearly seen. Over the core region, the profiles of the mean velocities are identified to be approximately linear with the slope 2Ω; the width of the region increases with the increase in N_τ, indicating the growth of irrotational zone with neutral stability.

As shown in Figures 4(a)–(c) for turbulence intensities, the overall tendency, albeit with some exceptions, is that the turbulence intensities are suppressed in the suction wall region and enhanced in the pressure wall region when the rotation number increases. Based on the analysis of the transport equations of Reynolds stress components, the characteristics of turbulence intensities are mainly ascribed to the productions related to the mean shear and rotational stress generation. However, it is noted that the streamwise intensity u'_{rms} is somewhat augmented at low rotation

DOI: 10.1002/fld

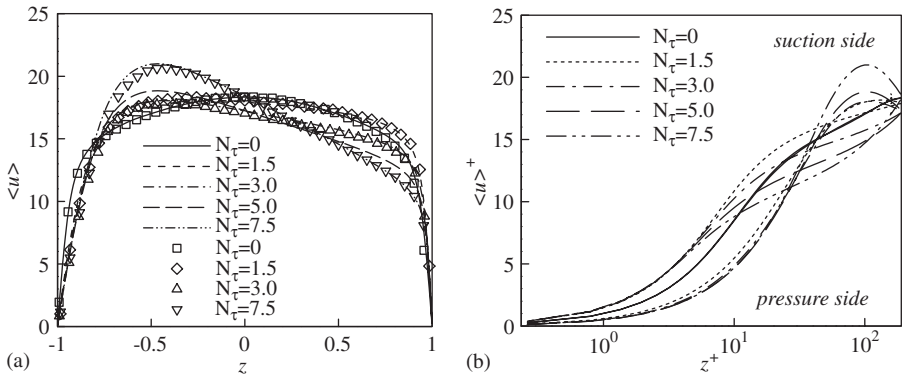

Figure 3. Profiles of the streamwise mean velocity: (a) streamwise mean velocity over the channel; and (b) streamwise mean velocity scaled by the global friction velocity.

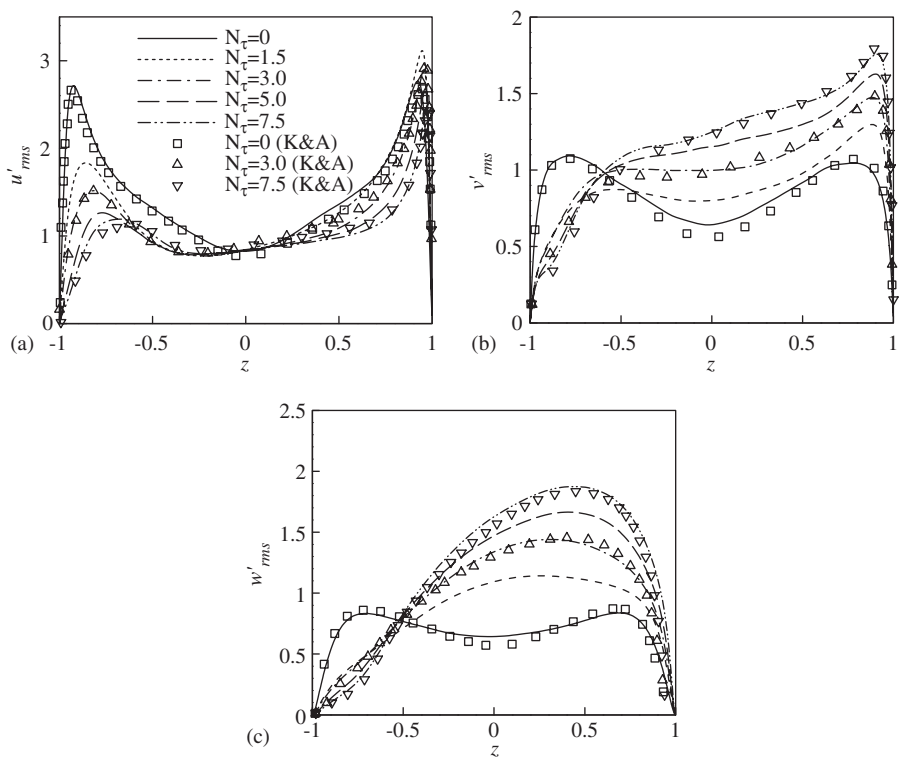

Figure 4. Turbulence statistics for different rotation numbers: (a) streamwise; (b) spanwise; and (c) wall-normal turbulence intensities.

number (e.g. $N_\tau = 1.5$) near the pressure wall, but greatly suppressed at high rotation number (e.g. $N_\tau = 7.5$), indicating notable restability of turbulence in the pressure wall region. This behaviour of the streamwise intensity near the pressure wall is much consistent with the previous data [6].

DOI: 10.1002/fld

4.2. Thermal statistics

Figure 5 shows the profiles of the mean temperature. From Figure 5(a), it is noted that the thickness of thermal diffusive sublayer near the suction side is larger than that near the pressure side. This behaviour is related to the fact that the turbulent flow is suppressed in the suction wall region and enhanced in the pressure wall region. In the core region, the mean temperature increases with the increase in N_τ. Since the rotational-induced Taylor–Görtler-like large-scale counter-rotating streamwise vortices (i.e. roll cells), which will be discussed below, are generated in the spanwise rotating channel, the presence of the large-scale structures enhances the transportation of high-temperature fluid from the pressure side into the core region. The distribution of the mean temperature in Figure 5(a) indicates that the molecular thermal diffusion related to the mean temperature gradient becomes weak in the core region of the rotating channel.

The profiles of the mean temperature, normalized by the friction temperature, are shown in Figure 5(b) in the logarithmic scale, where the mean temperature is described as

$$\langle T^+ \rangle = [\langle T \rangle - T|_{z=-1}]/T_\tau \quad \text{near the suction wall} \tag{4a}$$

$$\langle T^+ \rangle = [T|_{z=1} - \langle T \rangle]/T_\tau \quad \text{near the pressure wall} \tag{4b}$$

where $T_\tau = (\kappa/u_\tau)(|\mathrm{d}\langle T \rangle/\mathrm{d}z|_\mathrm{w})$ represents the friction temperature, and the subscript w denotes the variable at the channel wall.

Similar to the mean velocity distribution, there exists a buffer layer followed by a logarithmic region in the profiles of $\langle T^+ \rangle$ in the rotating cases. Then, by examining the data shown in Figure 5(b), the temperature profiles have a logarithmic form,

$$\langle T^+ \rangle = (1/K) \ln z^+ + B \tag{5}$$

where K and B represent the von Kárman and the additive constants, respectively. Based on the logarithmic fits to the temperature profiles in Figure 5(b), it is found that K and B depend on N_τ, which is closely relevant to the turbulent flow influenced by the destabilization (or stabilization) of flow in the pressure (or suction) wall region. As an analogy between the influences of rotation and thermal stratification on turbulent flows [3], the tendency of near-wall turbulent heat

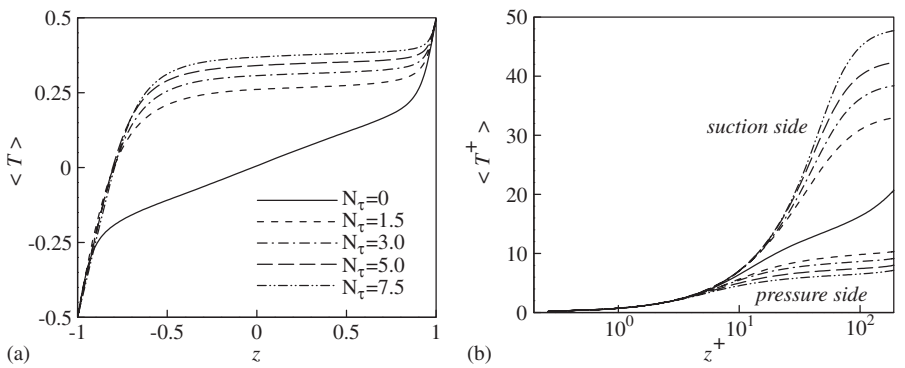

Figure 5. Profiles of the mean temperature: (a) mean temperature over the channel; and (b) mean temperature scaled by the friction temperature.

DOI: 10.1002/fld

transfer due to stabilization or destabilization is similar to the stably and unstably stratified turbulent flows [34].

Furthermore, it is seen from Figure 5(b) that $\langle T^+ \rangle$ is augmented considerably near the suction wall but suppressed appreciably near the pressure wall as the rotation rate increases, corresponding to the growth and diminishment of the region with large mean temperature gradient, respectively. The behaviour of $\langle T^+ \rangle$ is reasonably associated with the presence of the large-scale roll cells transporting high-temperature fluid from the pressure side to the core region. Consequently, the large-scale roll cells have a significant influence on the generation of the temperature fluctuation and turbulent heat flux in the spanwise rotating channel.

The Nusselt number is an important parameter relevant to the heat transfer coefficient at the wall and is defined as

$$Nu = \frac{q_w h}{k \Delta T} \tag{6}$$

where q_w denotes the mean heat flux at the channel wall, and k is the thermal conductivity. As exhibited in Figure 6, Nu decreases somewhat with the increase in N_τ, indicating that the rotation effect suppresses the wall-normal heat flux across the rotating channel.

The profiles of the temperature fluctuation, i.e. T'^+_{rms}, normalized by the friction temperature T_τ, are shown in Figure 7(a). The peak value of T'^+_{rms} on the suction side is higher than that on the pressure side. On the suction side, the temperature fluctuation is strengthened significantly due to the effect of rotation. Then, as N_τ increases, T'^+_{rms} is reduced gradually with the position of its peak value shifting away from the suction wall, indicating the thickening of thermal diffusive sublayer. Even at high rotation number (e.g. $N_\tau = 7.5$), T'^+_{rms} is greater than that for the non-rotating case near the suction wall. On the pressure side, T'^+_{rms} decreases monotonically with the increase in N_τ. The effect of rotation remarkably suppresses the temperature fluctuation near the pressure wall.

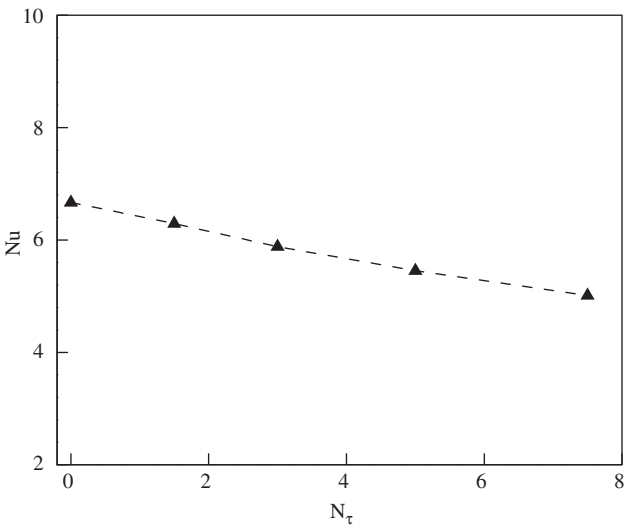

Figure 6. Nusselt number *versus* the rotation number.

DOI: 10.1002/fld

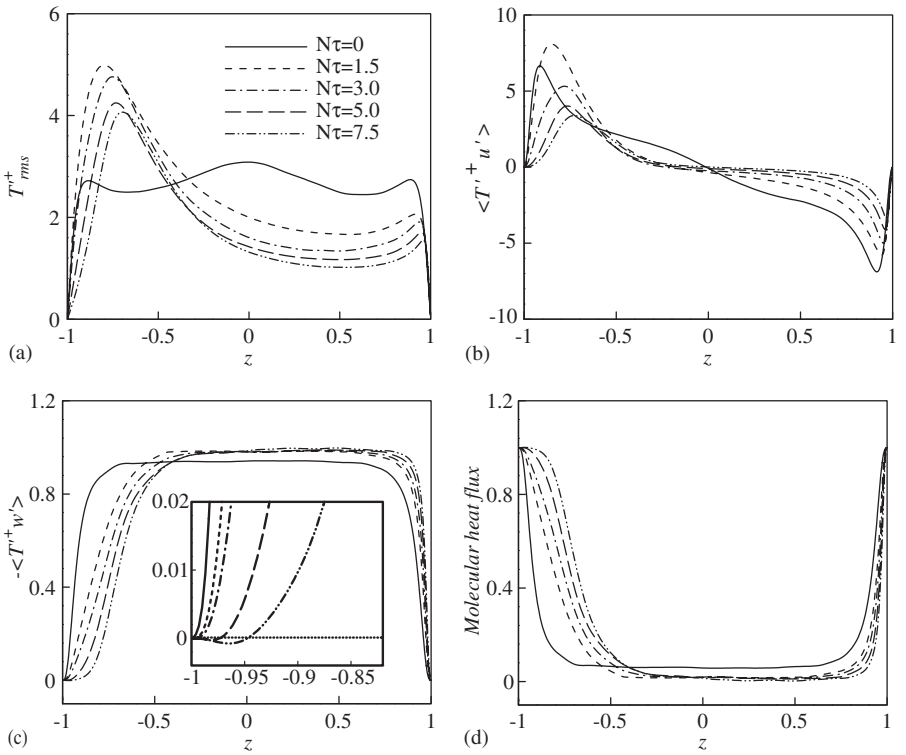

Figure 7. Thermal statistics: (a) temperature fluctuation; (b) streamwise turbulent heat flux; (c) wall-normal turbulent heat flux; and (d) molecular heat flux.

The behaviours of T'^+_{rms} will be analysed further in the following to reveal its relation to the large-scale roll cells.

The profiles of the streamwise turbulent heat flux (i.e. $\langle T'^+u'\rangle$) are shown in Figure 7(b). Similar to the behaviour of the temperature fluctuation in Figure 7(a), $\langle T'^+u'\rangle$ is strengthened at low rotation number (e.g. $N_\tau = 1.5$) due to the effect of rotation on the suction side. With the increase in N_τ, the peak value of $\langle T'^+u'\rangle$ decreases apparently and its position is away from the suction wall. Correspondingly, the absolute value of $\langle T'^+u'\rangle$ on the pressure side decreases as the rotation rate increases; it means that the poor correlation between the temperature and streamwise velocity fluctuations is mainly due to the suppression of the temperature fluctuation in Figure 7(a). The near-wall behaviour of $\langle T'^+u'\rangle$ represents that the sweep events with high-speed fluid rushing into the buffer layer are more probably characterized by positive temperature fluctuation in the suction wall region but by negative temperature fluctuation in the pressure wall region. Similarly, the burst events also play an important role on turbulent heat transfer in the boundary layer.

As shown in Figure 7(c) for the profiles of the wall-normal turbulent heat flux (i.e. $-\langle T'^+w'\rangle$), as N_τ increases, $-\langle T'^+w'\rangle$ decreases due to turbulence suppression on the suction side. However, on the pressure side, compared to the non-rotating case, $-\langle T'^+w'\rangle$ is somewhat enhanced subject

DOI: 10.1002/fld

to system rotation. At low rotation number, e.g. $N_\tau = 1.5$ and 3.0, the profiles of $-\langle T'^+ w' \rangle$ keep positive over the channel. As N_τ increases (e.g. $N_\tau = 5.0$ and 7.5), a minor negative value of $-\langle T'^+ w' \rangle$ appears very close to the suction wall. This feature should be attributed to the secondary flow induced by local roll cells, which is exhibited in the following.

Since a fully developed turbulent flow is assumed, the statistical thermal equilibrium is achieved with a relationship [9, 10],

$$\frac{1}{Re_\tau Pr}\left\langle \frac{\partial T^+}{\partial z} \right\rangle - \langle T'^+ w' \rangle = 1 \tag{7}$$

The first term on the left-hand side represents the heat flux related to the molecular thermal diffusion, and the second one is the wall-normal turbulent heat flux. Thus, Equation (7) represents the fact that the total heat flux across the channel is the sum of the molecular and the wall-normal turbulent heat flux. To specify the portions of both the terms in Equation (7) occupied in the total wall-normal heat flux in the rotating cases, the profiles of the molecular heat flux are shown in Figure 7(d). It is confirmed that the sum of the wall-normal turbulent heat flux (Figure 7(c)) and the molecular (Figure 7(d)) agrees well with the theoretical prediction in Equation (7). This behaviour also ensures that the temperature field is fully developed and the present calculation is accurately reliable.

As shown in Figures 7(c) and (d), in the suction wall region, the wall-normal turbulent heat flux levels off as N_τ increases, while the contribution of the molecular diffusion to the total wall-normal heat flux increases correspondingly in Figure 7(d). It means that the molecular heat flux is enhanced due to the thickening of the region with large gradient of mean temperature in Figure 5(a). However, near the pressure wall, the contribution of the turbulent motion to the total wall-normal heat flux slightly increases in Figure 7(c). Therefore, the resultant portion of the wall-normal heat flux due to the molecular diffusion is reduced slightly in the pressure wall region in Figure 7(d). At $N_\tau = 0$, $-\langle T'^+ w' \rangle$ is somewhat below unity in the core region in Figure 7(c); it is because, as shown in Figure 5(a), the non-zero mean temperature gradient appears. When the system rotation is imposed, Figure 7(c) exhibits that $-\langle T'^+ w' \rangle$ is nearly equal to unity in the core region, taking major responsibility for heat transfer in the wall-normal direction. Thus, it is identified that the wall-normal heat flux is mainly contributed by the molecular diffusion in the near-wall regions and by the turbulent motion in the core region.

4.3. Thermal budgets

To examine the effect of system rotation on turbulent heat transfer, it is needed to analyse the budget terms in the transport equations of turbulent heat fluxes $\langle T' u_i' \rangle$, which are given in Appendix by taking ensemble average on Equations (2) and (3) [39]. Due to the inhomogeneity introduced by the wall and the system rotation, the terms in the budgets have a strong dependence on the distance from the wall and the primary balance involves different terms at different heights.

It is noted that, as shown in Equation (A1), the budgets of the wall-normal and streamwise turbulent heat fluxes are coupled with each other by the Coriolis force terms, which are represented as $N_\tau \langle T' u' \rangle$ and $-N_\tau \langle T' w' \rangle$, respectively. Thus, in the spanwise rotating channel flow, the wall-normal turbulent heat flux contributes to the generation of the streamwise turbulent heat flux directly via the Coriolis force, and vice versa.

Here, the budget terms in the transport equation of the wall-normal turbulent heat flux, i.e. $\langle T' w' \rangle$, are mainly discussed. Figure 8 shows the profiles of the budget terms at $N_\tau = 0$ and 5.0. The

DOI: 10.1002/fld

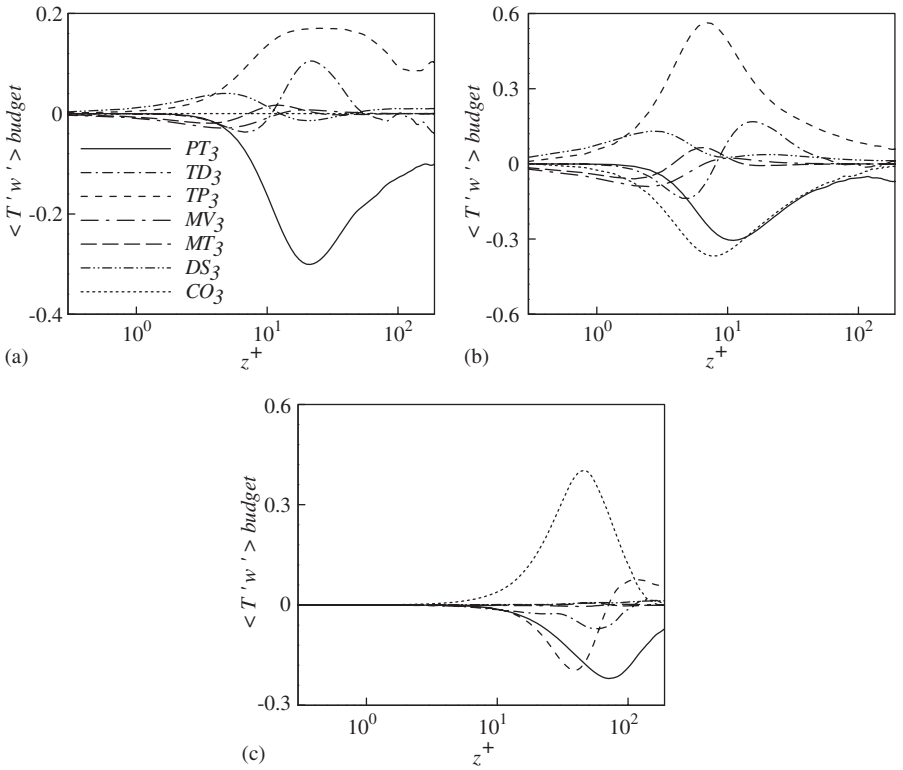

Figure 8. Distributions of the budget terms in the transport equation of $\langle T'^{+}w'\rangle$: (a) $N_\tau = 0$; (b) $N_\tau = 5.0$, near the pressure wall; and (c) $N_\tau = 5.0$, near the suction wall.

production rate due to the mean velocity gradient PV_3 vanishes since the mean wall-normal velocity is always zero. As shown in Figure 8(a) for $N_\tau = 0$, the temperature pressure gradient correlation term TP_3 is dominant acting as a source term to generate the wall-normal turbulent heat flux (i.e. $\langle T'w'\rangle$), which is consistent with the findings for the non-rotating channel flow [9, 10]. Both the production rate due to the mean temperature gradient PT_3 and the turbulent diffusion TD_3 also play major contribution to the budget balance. Thus, the balance is achieved mainly among TP_3, PT_3 and TD_3. The dissipation rate DS_3 is relatively small because of the isotropy in the dissipation scale [9]. As system rotation is imposed, as shown in Figures 8(b) and (c), the non-zero Coriolis force term CO_3 arises and becomes comparable to TP_3 and PT_3. On the pressure side (Figure 8(b)), TP_3 is augmented greatly and balanced with the rotational-enhanced PT_3 and CO_3. The negative CO_3 prevails over PT_3 and serves as a sink term in the budget balance. On the suction side (Figure 8(c)), it is noted that TP_3 reverses its sign to be negative due to the presence of system rotation, and CO_3 exhibits notably large positive value and is mainly responsible for the generation of the wall-normal turbulent heat flux.

To illustrate the rotation effect on the budget terms, Figure 9 shows the distributions of both typical terms, i.e. TP_3 and CO_3, at different rotation numbers. In Figure 9(a), the peak value of TP_3 is gradually enhanced with the increase in N_τ, with its location shifting towards the

DOI: 10.1002/fld

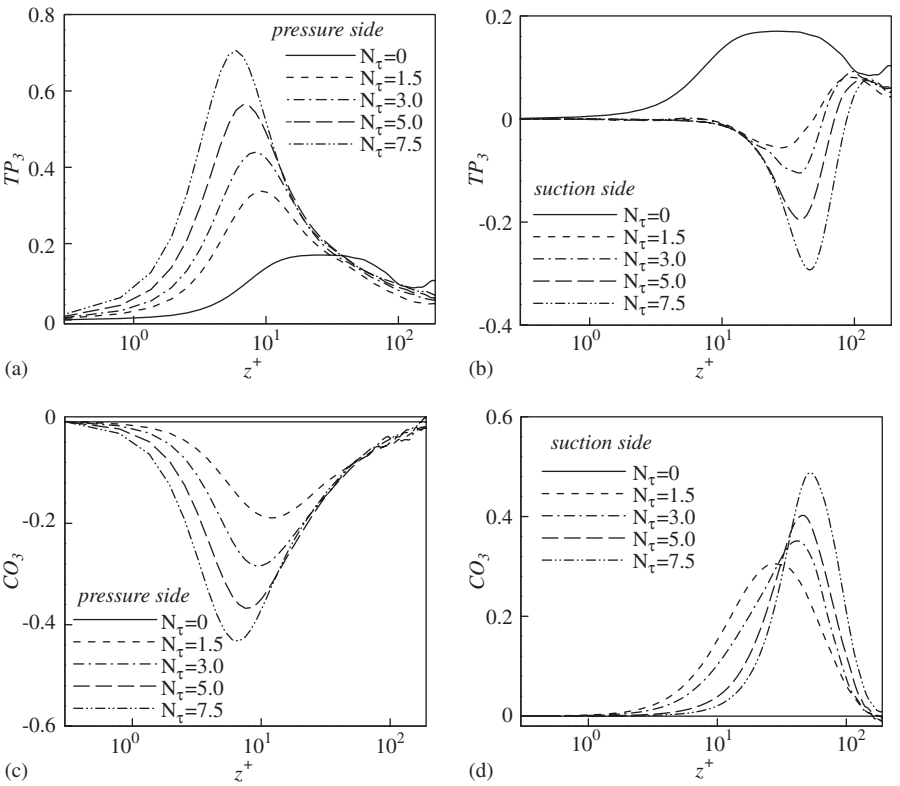

Figure 9. Budget terms in the transport equation of $\langle T'^{+}w'\rangle$: (a) TD_3, near the pressure wall; (b) TD_3, near the suction wall; (c) CO_3, near the pressure wall; and (d) CO_3, near the suction wall.

pressure wall. This behaviour is consistent with the profiles of the wall-normal turbulent heat flux near the pressure wall in Figure 7(c). The increase in TP_3 on the pressure side is mainly due to the rotational-enhanced value of CO_3, as shown in Figure 9(c), based on the balance of the $\langle T'w'\rangle$ budget in Figure 8. As shown in Figure 9(b), the sign reversion of TP_3 appears on the suction side. The magnitude of TP_3 increases as the rotation rate increases, in order to balance the rotational-enhanced CO_3 in the $\langle T'w'\rangle$ budget shown in Figure 9(d).

4.4. Large-scale structures

In the spanwise rotating channel flow, the rotational-induced Taylor–Görtler-like large-scale counter-rotating streamwise vortices (i.e. the roll cells) are generated. The secondary flow in the cross-sectional plane induced by these roll cells contributes roughly 25% of the kinetic energy and is associated with the streaky structures in the wall region [6]. As indicated above, these large-scale roll cells play an important role on turbulent heat transfer. To reveal the mechanisms related to the large-scale structures, based on the procedure [6], the instantaneous velocity and temperature fluctuations can be decomposed into the contributions from the large-scale roll cells

DOI: 10.1002/fld

and the real turbulent fluctuations, denoted by the subscripts c and r, respectively,

$$u_i' = u_{ci}' + u_{ri}', \quad T' = T_c' + T_r' \tag{8}$$

Here, the contributions from the large-scale roll cells, u_{ci}' and T_c', are obtained by averaging the instantaneous velocity and temperature fluctuations in the streamwise direction and in time [6]. Consequently, the temperature variance and the turbulent heat flux can be expressed as

$$\langle T'^{+2} \rangle = \langle (T_c'^{+} + T_r'^{+})^2 \rangle = \langle T_c'^{+2} \rangle + \langle T_r'^{+2} \rangle \tag{9}$$

$$\langle T'^{+} u_i' \rangle = \langle (T_c'^{+} + T_r'^{+})(u_{ci}' + u_{ri}') \rangle = \langle T_c'^{+} u_{ci}' \rangle + \langle T_r'^{+} u_{ri}' \rangle \tag{10}$$

The decompositions for the temperature variance and the turbulent heat flux only make sense in the situations where the large-scale roll cells are persistent [6]. Then, the first terms on the right-hand sides of Equations (9) and (10) represent the contributions from the large-scale roll cells, and the last terms from the real turbulent fluctuation.

Figure 10 shows the large-scale roll cells in the cross-sectional plane at $N_\tau = 1.5$ and 7.5, and the corresponding patterns of the temperature fluctuation and the wall-normal turbulent heat transfer. As shown in Figures 10(a) and (b), the persistent large-scale roll cells are clearly identified. The large-scale structures are adjacent to the pressure wall and extend up to the most cross-sectional region. The velocity vectors and streamlines indicate clearly that the secondary flow away from the pressure wall, which convects high-temperature fluid from the pressure side to the core region, is relatively stronger compared with the return flow. This behaviour is responsible for the high

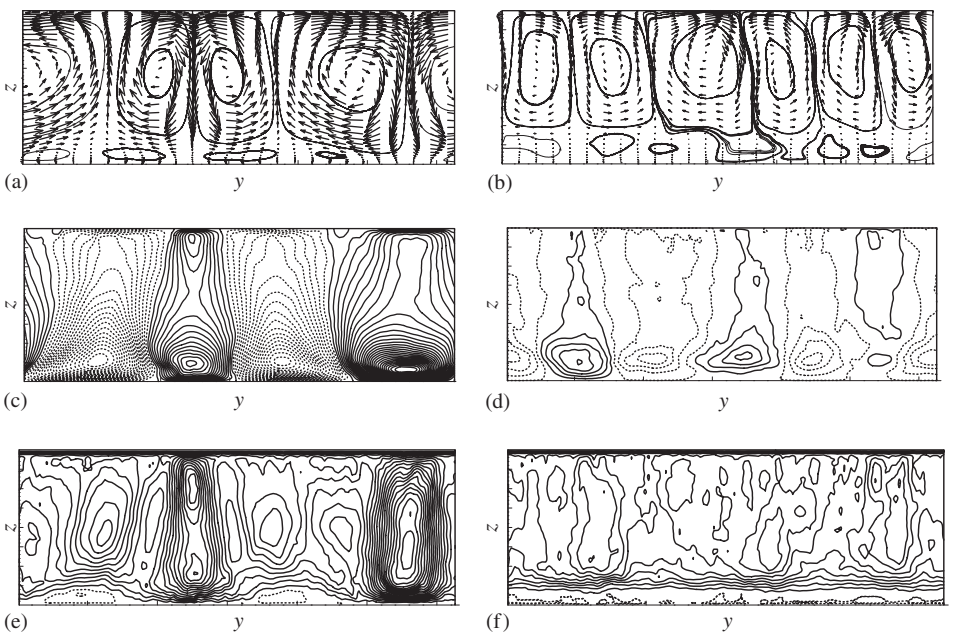

Figure 10. Patterns of large-scale roll cells for: (a) $N_\tau = 1.5$; and (b) $N_\tau = 7.5$. Contour plots of $T_c'^{+}$ for: (c) $N_\tau = 1.5$; and (d) $N_\tau = 7.5$. Contour plots of $-T_c'^{+} w_c'$ for: (e) $N_\tau = 1.5$; and (f) $N_\tau = 7.5$.

DOI: 10.1002/fld

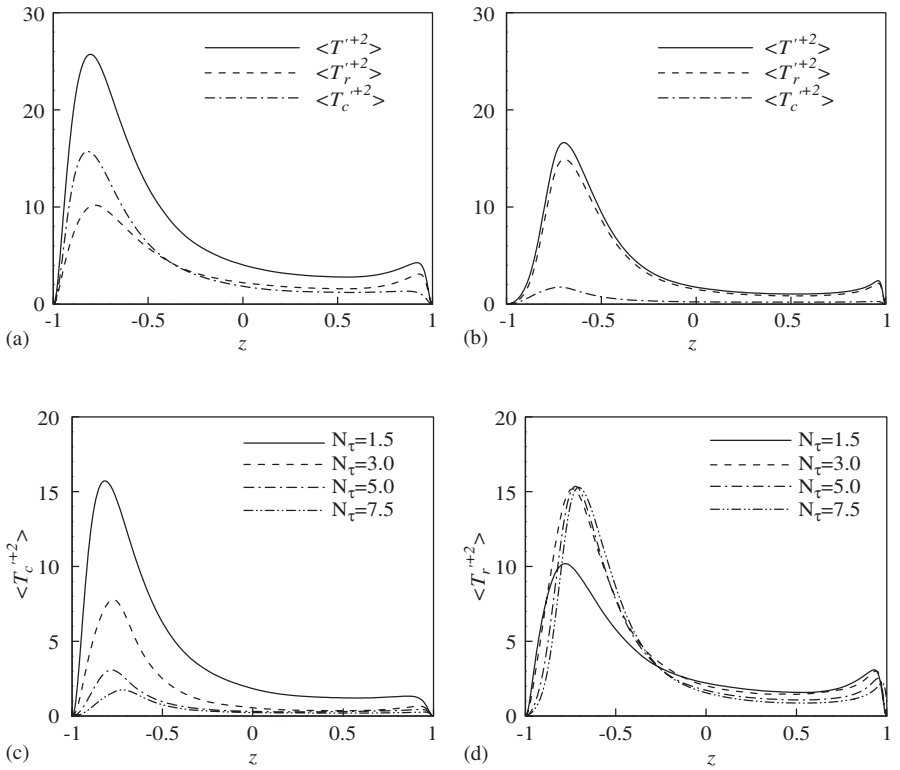

Figure 11. Decomposition of the temperature variance: (a) $N_\tau = 1.5$; (b) $N_\tau = 7.5$; (c) contribution from the large-scale roll cells for different rotation numbers; and (d) contribution from the real temperature fluctuation.

mean temperature profile over the core region of the rotating channel in Figure 5(a). As N_τ varies from 1.5 to 7.5, the number of these roll cells increases from 4 to 6 due to the Taylor–Görtler instability. It is reasonably predicted that the increase in the number of roll cells also can enhance high-temperature fluid convecting from the pressure side to the core region. Consequently, as shown in Figure 5(a), the mean temperature over the core region increases with the increase in N_τ. Furthermore, the local roll cells induced by the large-scale roll cells, which are much weak compared to the large-scale ones, occur close to the suction wall and become somewhat strong at high rotation number. The weak secondary flow induced by the local roll cells is then conjectured to affect thermal statistics close to the suction wall, e.g. as shown in Figure 7(c) where a minor negative value of $-\langle T'^{+} w' \rangle$ occurs very close to the suction wall.

As shown in Figures 10(c) and (d) for the patterns of $T_c'^{+}$ at $N_\tau = 1.5$ and 7.5, respectively, it is observed that dense contour lines appear near the suction wall, but sparse ones are close to the pressure wall. The contours clearly indicate that $T_c'^{+}$ becomes weak with the increase in N_τ. The number of the large-scale roll cells based on $T_c'^{+}$ is reasonably identified and is consistent with the structures in Figures 10(a) and (b). Correspondingly, the patterns of the wall-normal turbulent heat flux due to the large-scale roll cells, i.e. $-(T_c'^{+} w_c')$, are also exhibited in Figures 10(e) and (f) for

DOI: 10.1002/fld

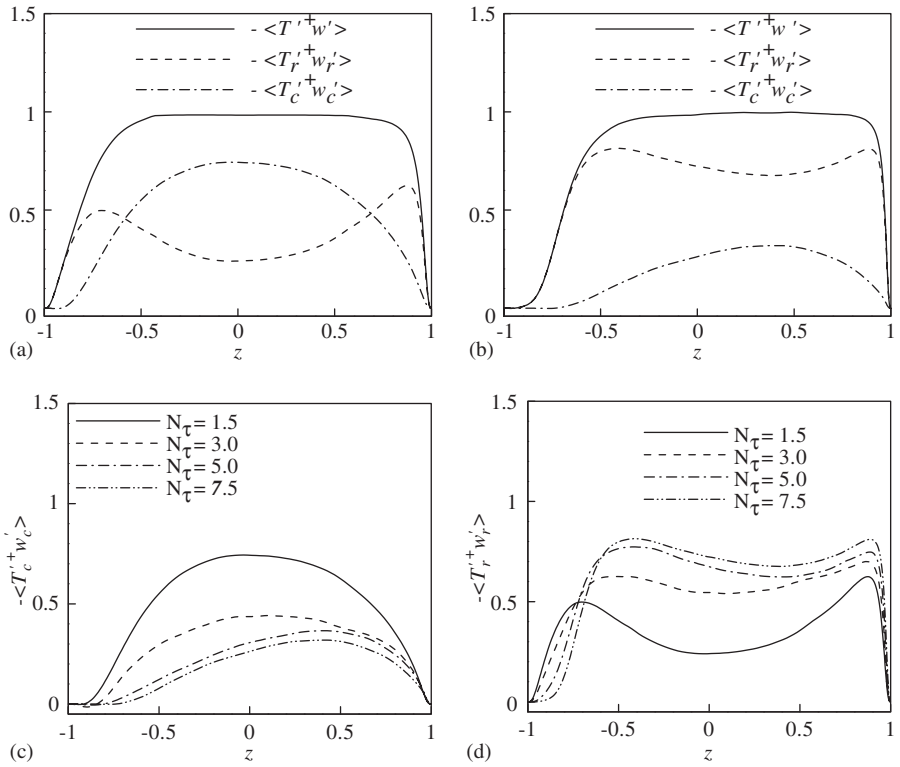

Figure 12. Decomposition of the wall-normal turbulent heat flux: (a) $N_\tau = 1.5$; (b) $N_\tau = 7.5$; (c) contribution from the large-scale roll cells for different rotation numbers; and (d) contribution from the real turbulent fluctuation.

$N_\tau = 1.5$ and 7.5. It is noted that minor negative values appear in the immediate neighbourhood of suction wall, and should be ascribed to the secondary flow induced by the local roll cells close to the suction wall in Figures 10(a) and (b). This behaviour is consistent with the statistical data in Figure 7(c).

To exhibit the influence of the large-scale structures on the temperature variance $\langle T'^{+2}\rangle$, Figures 11(a) and (b) show the profiles of the decompositions of $\langle T'^{+2}\rangle$ for $N_\tau = 1.5$ and 7.5, respectively. In weak rotating case, e.g. $N_\tau = 1.5$ (Figure 11(a)), the large-scale roll cells contribute the most to $\langle T'^{+2}\rangle$, and the profile of $\langle T_c'^{+2}\rangle$ prevails over that of $\langle T_r'^{+2}\rangle$ in the suction wall region. Therefore, the feature of $\langle T_c'^{+2}\rangle$ is responsible for the remarkable increase in the temperature fluctuation near the suction wall for $N_\tau = 1.5$ in Figure 7(a). However, in the pressure wall region, the contribution of $\langle T_c'^{+2}\rangle$ is relatively small. At high rotation number, e.g. $N_\tau = 7.5$ (Figure 11(b)), it is shown that $\langle T_c'^{+2}\rangle$ is nearly negligible, compared with $\langle T_r'^{+2}\rangle$; the temperature variance is thus dominated by the real temperature fluctuation.

Further, as shown in Figure 11(c) for $\langle T_c'^{+2}\rangle$, with the increase in N_τ, the contribution from the large-scale roll cells to $\langle T'^{+2}\rangle$ is reduced significantly, in particular, in the suction wall region. On the other hand, in the suction wall region, the contribution due to $\langle T_r'^{+2}\rangle$ increases sharply when N_τ changes from 1.5 to 3.0 in Figure 11(d). Then, the profiles of $\langle T_r'^{+2}\rangle$ are very similar to each

DOI: 10.1002/fld

other when N_τ increases from 3.0 to 7.5. In the pressure wall region, however, $\langle T_r'^{+2}\rangle$, compared to $\langle T_c'^{+2}\rangle$, contributes the most to $\langle T'^{+2}\rangle$ for the rotating cases.

The wall-normal turbulent heat flux is decomposed to explore the influence of the large-scale roll cells. The decomposed portions, i.e. $-\langle T_c'^{+} w_c'\rangle$ and $-\langle T_r'^{+} w_r'\rangle$, are exhibited in Figures 12(a) and (b) for $N_\tau = 1.5$ and 7.5, respectively. As shown in Figure 12(a) for $N_\tau = 1.5$, $-\langle T_c'^{+} w_c'\rangle$ is considerably large in the core region, but becomes small in the wall regions. This observation therefore indicates that the large-scale roll cells give considerable contribution to $-\langle T'^{+} w'\rangle$ in the core region, and $-\langle T_r'^{+} w_r'\rangle$ plays a dominant contribution to $-\langle T'^{+} w'\rangle$ in the wall regions. In Figure 12(b) for $N_\tau = 7.5$, the contribution due to the large-scale roll cells $-\langle T_c'^{+} w_c'\rangle$ reduces obviously; correspondingly, the contribution due to the real turbulent fluctuation $-\langle T_r'^{+} w_r'\rangle$ increases. Figures 12(c) and 10(d) show the profiles of $-\langle T_c'^{+} w_c'\rangle$ and $-\langle T_r'^{+} w_r'\rangle$ for different rotation numbers. It is noted that the contribution due to $-\langle T_r'^{+} w_r'\rangle$ increases with the increase in N_τ, but the contribution due to $-\langle T_c'^{+} w_c'\rangle$ decreases.

5. CONCLUDING REMARKS

The spanwise rotating turbulent channel flow with heat transfer has been studied by means of DNS. To examine the effect of system rotation on the characteristics of turbulent flow, heat transfer, and large-scale motions, some statistical quantities, including the mean velocity, temperature and their fluctuations, turbulent heat fluxes, and the structures of the velocity and temperature fluctuations, are analysed. Turbulence intensities are reduced on the suction side while enhanced on the pressure side due to the effect of rotation. The mean temperature is augmented considerably near the suction wall and suppressed appreciably near the pressure wall, corresponding to the growth and diminishment of the region with large mean temperature gradient, respectively. The Nusselt number decreases somewhat as the rotation rate increases, indicating that the rotation effect suppresses the wall-normal heat flux across the rotating channel. On the suction side, the thermal statistics are strengthened significantly due to the presence of system rotation and reduced with the increase in the rotation number. On the pressure side, the thermal statistics are suppressed. The wall-normal heat flux due to turbulent motion is weak near the suction wall but becomes relatively strong near the pressure wall. The wall-normal heat flux is contributed mainly from the molecular diffusion in the near-wall regions and from the turbulent motion in the core region. The generation of the wall-normal and streamwise turbulent heat fluxes are coupled with each other via the Coriolis force in the transport equations of turbulent heat fluxes. The rotational-induced Coriolis force term plays an important role in the budget balance of the wall-normal turbulent heat flux, as a sink term on the pressure side but a source term on the suction side. The decomposition of the velocity fluctuations shows clearly the existence of large-scale roll cells in the cross-sectional plane. Based on the analysis of the decomposition of thermal statistical quantities, the large-scale structures have a significant influence on the thermal statistics.

APPENDIX A: EQUATIONS FOR TURBULENT HEAT FLUXES

The transport equation for the turbulent heat fluxes $\langle T' u_i'\rangle$ can be written as

$$\frac{\partial\langle T' u_i'\rangle}{\partial t} + \langle u_j\rangle \frac{\partial\langle T' u_i'\rangle}{\partial x_j} = \mathrm{PV}_i + \mathrm{PT}_i + \mathrm{TP}_i + \mathrm{TD}_i + \mathrm{MV}_i + \mathrm{MT}_i + \mathrm{DS}_i + \mathrm{CO}_i \tag{A1}$$

DOI: 10.1002/fld

The terms on the right-hand side are expressed as:

$\mathrm{PV}_i = -\langle u'_j T' \rangle \partial \langle u_i \rangle / \partial x_j$, production rate by mean velocity gradient;
$\mathrm{PT}_i = -\langle u'_i u'_j \rangle \partial \langle T \rangle / \partial x_j$, production rate by mean temperature gradient;
$\mathrm{TP}_i = -\langle T'(\partial p'/\partial x_i) \rangle$, temperature pressure gradient correlation;
$\mathrm{TD}_i = -\partial \langle u'_i u'_j T' \rangle / \partial x_j$, turbulent diffusion;
$\mathrm{MV}_i = \langle \partial / \partial x_j [T'(\partial u'_i / \partial x_j)] \rangle / Re_\tau$, molecular diffusion relevant to velocity fluctuation;
$\mathrm{MT}_i = \langle \partial / \partial x_j [u'_i (\partial T' / \partial x_j)] \rangle / (Re_\tau Pr)$, molecular diffusion relevant to temperature fluctuation;
$\mathrm{DS}_i = -[1/Re_\tau + 1/(Re_\tau Pr)] \langle (\partial u'_i / \partial x_j)(\partial T' / \partial x_j) \rangle$, dissipation rate; and
$\mathrm{CO}_i = -\varepsilon_{ijk}(N_\tau / Re_\tau)(\Omega_j / \Omega) \langle u'_k T' \rangle$, Coriolis force term.

ACKNOWLEDGEMENTS

This work was supported by the National Natural Science Foundation of China (No. 10302028 and No. 90405007), the Hundred Talents Program of the Chinese Academy of Sciences, and Program for Changjiang Scholars and Innovative Research Team in University.

REFERENCES

1. Matsubara M, Alfredsson PH. Experimental study of heat and momentum transfer in rotating channel flow. *Physics of Fluids* 1996; **8**:2964–2973.
2. Sha WM, Tsuchiya K, Nakabayashi K. The linear stability of thermally stratified rotating channel flow. *Physics of Fluids* 1999; **11**:439–449.
3. Johnston JP, Halleen RM, Leziius DK. Effects of spanwise rotation on the structure of two-dimensional fully developed turbulent channel flow. *Journal of Fluid Mechanics* 1972; **56**:533–557.
4. Nakabayashi K, Kitoh O. Low Reynolds number fully developed turbulent channel flow with system rotation. *Journal of Fluid Mechanics* 1996; **315**:1–29.
5. Piomelli U, Liu J. Large-eddy simulation of rotating channel flows using a localized dynamic model. *Physics of Fluids* 1995; **7**:839–848.
6. Kristoffersen R, Andersson HI. Direct simulations of low-Reynolds number turbulent flow in a rotating channel. *Journal of Fluid Mechanics* 1993; **235**:163–197.
7. Lamballais E, Metais O, Leiseur M. Spectral-dynamical model for large-eddy simulations of turbulent rotating channel flow. *Theoretical and Computational Fluid Dynamics* 1998; **12**:149–177.
8. Wu HB, Kasagi N. Effects of arbitrary directional system rotation on turbulent channel flow. *Physics of Fluids* 2004; **16**:979–990.
9. Kawamura H, Ohsaka K, Abe H, Yamamoto K. DNS of turbulent heat transfer in channel flow with low to medium-high Prandtl number fluid. *International Journal of Heat and Fluid Flow* 1998; **19**:482–491.
10. Kawamura H, Abe H, Matsuo Y. DNS of turbulent heat transfer in channel flow with respect to Reynolds and Prandtl number effects. *International Journal of Heat and Fluid Flow* 1999; **20**:196–207.
11. Nagano Y, Hattori H. Direct numerical simulation and modelling of spanwise rotating channel flow with heat transfer. *Journal of Turbulence* 2003; **4**(10):1–15.
12. Kim J, Moin P. Transport of passive scalars in a turbulent channel flow. *Turbulent Shear Flows* 1989; **6**:85–96.
13. Lyons SL, Hanratty TJ, Mclaughlin JB. Direct numerical simulation of passive heat transfer in a turbulent channel flow. *International Journal of Heat and Mass Transfer* 1991; **34**:1149–1161.
14. Kasagi N, Tomita Y, Kuroda A. Direct numerical simulation of passive scalar field in a turbulent channel flow. *Journal of Heat Transfer* (ASME) 1992; **144**:598–606.
15. Kasagi N, Ohtsubo Y. Direct numerical simulation of low Prandtl number thermal filed in a turbulent channel flow. *Turbulent Shear Flows* 1993; **8**:97–119.
16. Nagano Y, Hattori H. An improved turbulence model for rotating shear flows. *Journal of Turbulence* 2002; **3**(6):1–14.
17. Verzicco R, Orlandi P. A finite difference scheme for direction simulation in cylindrical coordinates. *Journal of Computational Physics* 1996; **123**:402–414.

DOI: 10.1002/fld

18. Kim J, Moin P. Application of a fractional-step method to incompressible Navier–Stokes equations. *Journal of Computational Physics* 1985; **59**:308–323.
19. Rai MM, Moin P. Direct simulations of turbulent flow using finite-difference schemes. *Journal of Computational Physics* 1991; **96**:15–53.
20. Kim J, Moin P, Moser R. Turbulence statistics in fully developed channel flow at low Reynolds number. *Journal of Fluid Mechanics* 1987; **177**:133–166.
21. Liu NS, Lu XY. A numerical investigation of turbulent flows in a spanwise rotating channel. *Computers and Fluids*, in press.
22. Orlandi P. Helicity fluctuations and turbulent energy production in rotating and non-rotating pipes. *Physics of Fluids* 1997; **9**:2045–2056.
23. Orlandi P, Ebstein D. Turbulent budgets in rotating pipes by DNS. *International Journal of Heat and Fluid Flow* 2000; **21**:499–505.
24. Orlandi P, Fatica M. Direct simulations of turbulent low in a pipe rotating about its axis. *Journal of Fluid Mechanics* 1997; **343**:43–72.
25. Pan YK, Tanaka T, Tsuji Y. Direct numerical simulation of particle-laden rotating turbulent channel flow. *Physics of Fluids* 2001; **13**:2320–2337.
26. Chung SY, Rhee GH, Sung HJ. Direct numerical simulation of turbulent concentric annular pipe flow. Part 1: flow field. *International Journal of Heat and Fluid Flow* 2002; **23**:426–440.
27. Vittor G, Verzicco R. Direct simulation of transition in an oscillatory boundary layer. *Journal of Fluid Mechanics* 1998; **371**:207–232.
28. Quadrio M, Sibilla S. Numerical simulation of turbulent flow in a pipe oscillating around its axis. *Journal of Fluid Mechanics* 2000; **424**:217–241.
29. Grossmann S, Lohse D. On geometry effects in Rayleigh–Bénard convection. *Journal of Fluid Mechanics* 2003; **486**:105–114.
30. Liu NS, Lu XY. Large eddy simulation of turbulent concentric annular channel flows. *International Journal for Numerical Methods in Fluids* 2004; **45**:1317–1338.
31. Dong YH, Lu XY. Large eddy simulation of a thermally stratified turbulent channel flow with temperature oscillation on the wall. *International Journal of Heat and Mass Transfer* 2004; **47**:2109–2122.
32. Wang L, Lu XY. An investigation of turbulent oscillatory heat transfer in channel flows by large eddy simulation. *International Journal of Heat and Mass Transfer* 2004; **47**:2161–2172.
33. Wang L, Dong YH, Lu XY. An investigation of turbulent open channel flow with heat transfer by large eddy simulation. *Computers and Fluids* 2005; **34**:23–47.
34. Lu XY, Wang SW, Sung HG, Hsieh SY, Yang V. Large eddy simulations of turbulent swirling flows injected into a dump chamber. *Journal of Fluid Mechanics* 2005; **527**:171–195.
35. Dong YH, Lu XY. Direct numerical simulation of stably and unstably stratified open channel flows. *Acta Mechanica* 2005; **177**:115–136.
36. Wang L, Lu XY. Large eddy simulation of stably stratified turbulent open channel flows with low- to high-Prandtl number. *International Journal of Heat and Mass Transfer* 2005; **48**:1883–1897.
37. Zou LY, Liu NS, Lu XY. An investigation of pulsating turbulent open channel flow. *Computers and Fluids* 2006; **35**:74–102.
38. Li BY, Liu NS, Lu XY. Direct numerical simulation of wall-normal rotating turbulent channel flow with heat transfer. *International Journal of Heat and Mass Transfer* 2006; **49**:1162–1175.
39. Mansour NN, Kim J, Moin P. Reynolds-stress and dissipation-rate budgets in a turbulent channel flow. *Journal of Fluid Mechanics* 1988; **194**:15–44.

DOI: 10.1002/fld